

## An insight into the electronic structure of graphene: from monolayer to multi-layer

Z.F.Wang,<sup>1</sup> Huaixiu Zheng,<sup>2</sup> Q.W. Shi,<sup>1</sup> Jie Chen,<sup>2</sup> Jinlong Yang,<sup>1</sup> and J.G. Hou<sup>1</sup><sup>1</sup>Hefei National Laboratory for Physical Sciences at Microscale,  
University of Science and Technology of China, Hefei, Anhui 230026, People's Republic of China<sup>2</sup>Electrical and Computer Engineering, University of Alberta, AB T6G 2V4, Canada

(Dated: March 23, 2024)

In this paper, we analytically investigate the electronic structure of Bernal stacking (AB stacking) graphene evolving from monolayer (a zero-gap semiconductor with a linear Dirac-like spectrum around the Fermi energy) to multi-layer (semimetal bulk graphite). We firstly derive a real space analytical expression for the free Green's function (propagator) of multi-layer graphene based on the effective-mass approximation. The simulation results exhibit highly spatial anisotropy with three-fold rotational symmetry. By combining with the STM measurement of  $d^2I/dV^2$  (the second derivative of current), we also provide a clear high-throughput and non-destructive method to identify graphene layers. Such a method is lacking in the emerging graphene research.

PACS numbers: 73.61Wp, 61.72.Ji, 68.37.Ef

## I. INTRODUCTION

The successful synthesis of monolayer graphite (graphene) has attracted enormous research interest over the past years.<sup>1</sup> Researchers can also experimentally manipulate few layer within multi-layer graphene samples and observe their quasi two-dimensional behavior.<sup>2,3,4,5,6,7</sup> The conduction band of graphene is well described by the tight-binding model, which includes the  $p_z$  orbitals that is perpendicular to the plane each carbon atom locates. This model describes a semimetal, with zero density of states at the Fermi energy. Here, the Fermi surface is reduced to two inequivalent  $K$ -points located at the corners of the hexagonal Brillouin Zone. The low-energy excitations with momenta in the vicinity of any Fermi points have a linear dispersion. They can be described by a continuous model, which reduces to the Dirac equation in two dimensions. These observations have been validated experimentally<sup>1</sup>.

Recent research attention has turned to study multi-layer graphene<sup>2,3,4,5,6,7</sup>, because its electronic properties are quite different from those of the monolayer graphene. Two-dimensional (2D) multi-layer graphene is an intermediate crystals between bulk graphite and a single graphene plane. Relatively weak inter-layer coupling within multilayer graphene inherits some properties from monolayer graphenes. The special geometry of the Bernal stacking (A-B stacking) between graphene layers results in low-energy states mainly reside around B site. In contrast to corresponding three-dimensional (3D) bulk structures, electrons in a multi-layer graphene are confined along one crystallographic direction, which offers its unique electronic characteristics. From the Hall effect measurements of a multi-layer graphene, the results show that multi-layer graphene behaves like multi-carriers (coexistence of electrons and holes) semimetallic systems.<sup>8,9</sup> Moreover, carriers can switch from electron to hole transport by altering gate voltage. This phenomenon makes multi-layer graphene a remarkable platform for studying mesoscopic transport in low-dimensional materials. It is also worth noting that multi-layer graphene system may be of interest for building nanoscale devices because we can easily change their electronic properties by using conventional lithographic techniques.

To date, few studies attempting to uncover the unique electronic properties of multi-layer graphene in an analytical fashion. Moreover, the physical properties of multi-layer graphene are closely related to its propagator. In this paper, we first develop an analytical formula of the free Green's function for electrons in multi-layer graphene (Bernal stacking) in real space by using the effective-mass approximation. We then calculate the LDOS of multi-layer graphene and isotropic function by using Green's function explicitly with increasing number of graphene layers. Our numerical results show that monolayer graphene is dramatically different from other multi-layer graphene, and bilayer graphene capture the main characters of the multi-layer graphene. Currently only AFM and Raman spectrum<sup>1,10,11</sup> are used to detect the layers of graphene. In this paper, we present an effective method to detect graphene layers based on the STM. According to our derivative of LDOS with energy (proportional to the second derivative of current  $d^2I/dV^2$ ), we can quickly, clearly and nondestructively identify the graphene layers of finite multi-layer graphene based on STM images.

## II. TIGHT-BINDING DESCRIPTION

Figure 1 shows schematically the crystal structure of four AB-stacked graphene layers and the corresponding first Brillouin zone with the labels of the symmetric points. It was shown in the reference [12] that the interplanar spacing

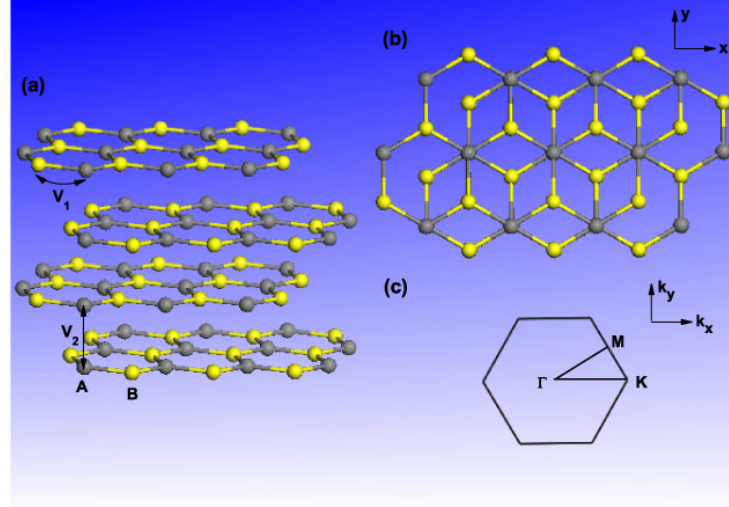


FIG. 1: (color online) The crystal structure of four AB stacked graphene layers. Type-A atoms (gray) have direct neighbors in the adjacent atomic layers while type-B atoms (yellow) are above hollow sites. (a) Side view with the corresponding tight-binding parameters, (b) Top view. (c) The first Brillouin zone of a finite number of graphene layers with the labels of special symmetric points (Here, we choose four-layer graphene as an example to illustrate our design).

parameter  $a$  and lattice spacing  $d$  in two-layer graphene are almost identical to that in bulk graphite. We, therefore, choose the bulk value  $a = 1.42\text{\AA}$  and  $d = 3.35\text{\AA}$  in this paper. In order to study how the electronic structure of graphene changes from monolayer into multi-layer, we construct the tight-binding Hamiltonian for an arbitrary number of graphene layers. We extend our previous studies of monolayer graphene<sup>13</sup> and of bilayer graphene<sup>14</sup> to multi-layer one. Starting from two-layer graphene, type A and B carbon atoms are inequivalent: type-A carbon atom has a direct neighbor in its adjacent layer while type-B carbon atom does not and locates on the hollow sites. Since the physical properties of graphene are determined by bands near the Dirac point, only the contribution from the band is considered in this paper. In our tight-binding model, we limit our calculation to the nearest interaction carbon atoms on the graphene's  $p_z$  orbitals. These interactions include interactions between the nearest A-B carbon atoms within a plane, interaction between nearest A-A carbon atoms of two nearest-neighbor planes. The tight-binding Hamiltonian of the multi-layer graphene is:

$$H = V_1 \sum_{l=1}^L \sum_{\langle ij \rangle} \psi_i^{l\dagger} \psi_j^l + V_2 \sum_{l=1}^L \sum_{\langle ll' \rangle} \psi_i^{l\dagger} \psi_j^{l'} \quad (1)$$

where  $\psi_i^{l\dagger}$  is the wavefunction at site  $i$  on layer  $l$ .  $L$  is the number of graphene layers.  $V_1$  is the nearest hopping parameter within the layer and  $V_2$  is the nearest hopping parameter between two layers. We select  $V_1 = 3.0\text{eV}$  and  $V_2 = 0.4\text{eV}$  in our calculation.

The Bloch orbits for two nonequivalent sites, A and B, on layer  $l$  are written as  $\psi_A^l = \frac{1}{N} \sum_{\mathbf{r}_A} e^{i\mathbf{k} \cdot \mathbf{r}_A} \psi_{\mathbf{r}_A}^l$ ,  $\psi_B^l = \frac{1}{N} \sum_{\mathbf{r}_B} e^{i\mathbf{k} \cdot \mathbf{r}_B} \psi_{\mathbf{r}_B}^l$ . The summation is over all sites A and B on layer  $l$ .  $\mathbf{r}_A$  and  $\mathbf{r}_B$  denote the real-space coordinates of A and B sites, respectively. Here,  $N$  is the number of unit cells in the crystal. The tight-binding Hamiltonian can be obtained from the following matrix elements:

$$\begin{aligned}
h_{k_A}^1 \psi_{k_A}^1 &= h_{k_B}^1 \psi_{k_B}^1 = 0; \\
h_{k_A}^1 \psi_{k_B}^1 &= \begin{matrix} V_1 & (l = \text{odd}) \\ V_1 & (l = \text{even}) \end{matrix}; \\
h_{k_B}^1 \psi_{k_A}^1 &= \begin{matrix} V_1 & (l = \text{odd}) \\ V_1 & (l = \text{even}) \end{matrix}; \\
h_{k_A}^1 \psi_{k_A}^{l+1} &= h_{k_A}^{l+1} \psi_{k_A}^1 = V_2:
\end{aligned} \tag{2}$$

with

$$= \exp(ik_y a) + \exp[i(-\frac{p-3ak_x}{2} - \frac{ak_y}{2})] + \exp[i(-\frac{p-3ak_x}{2} - \frac{ak_y}{2})]:$$

In these calculations, we neglect all overlap integrals because of the relatively large separation between the carbon atoms. Furthermore, we are only interested in small energy electronic structure around the K point. With the expressions in Eq (2), we can construct the tight-binding Hamiltonian for an arbitrary number of layers

$$H = \begin{pmatrix} 0 & 0 & V_1 & V_2 & 0 & 1 \\ V_1 & 0 & 0 & 0 & 0 & \vdots \\ V_2 & 0 & 0 & 0 & V_1 & \vdots \\ 0 & 0 & 0 & V_1 & 0 & \vdots \\ \vdots & \vdots & \vdots & \vdots & \vdots & \vdots \end{pmatrix} : \tag{3}$$

The eigenfunction for multi-layer graphene system is now given by

$$\psi = \sum_{l=1}^{L-1} \psi_A^l + \sum_{l=1}^{L-1} \psi_B^l : \tag{4}$$

The hopping between sublattices of different layer lead to the coupled Harper equations,

$$\begin{aligned}
\psi_A^l &= V_2 \psi_A^{l+1} + V_1 \psi_B^l + V_2 \psi_A^{l-1} \\
\psi_B^l &= V_1 \psi_A^l
\end{aligned} \quad (l = \text{odd}): \tag{5}$$

and

$$\begin{aligned}
\psi_A^l &= V_2 \psi_A^{l+1} + V_1 \psi_B^l + V_2 \psi_A^{l-1} \\
\psi_B^l &= V_1 \psi_A^l
\end{aligned} \quad (l = \text{even}): \tag{6}$$

where  $l = 1; 2; \dots; L$  denotes the layer number. The open boundary condition in the direction perpendicular to the 2D graphene plane is  $\psi_A^0 = \psi_A^{L+1} = \psi_B^0 = \psi_B^{L+1} = 0$ . According to the coupled Harper equations Eq.(5) and Eq.(6), the wave functions of the eigenstates and the corresponding energy spectrum can be obtained in the following analytical form.

$$\psi_m^s(k) = V_2 \cos(\frac{m}{L+1}) + s \sqrt{V_2^2 \cos^2(\frac{m}{L+1}) + V_1^2} \tag{7}$$

$$\begin{aligned}
\psi_A^l(m; s; k) &= D(m; s; k) \sin(\frac{ml}{L+1}); \\
\psi_B^l(m; s; k) &= \begin{cases} D(m; s; k) \frac{V_1}{\psi_m^s(k)} \sin(\frac{ml}{L+1}) & (l = \text{odd}) \\ D(m; s; k) \frac{V_1}{\psi_m^s(k)} \sin(\frac{ml}{L+1}) & (l = \text{even}) \end{cases};
\end{aligned} \tag{8}$$

where  $D(m; s; k) = \sqrt{\frac{2}{L+1} [1 + \frac{V_1^2}{\psi_m^s(k)^2}] \sin^2(\frac{m}{L+1})} g^{1/2}$  is the normalized factor ( $m = 1; 2; \dots; L$ ) and  $s = \pm 1$ .

### III. REAL-SPACE GREEN'S FUNCTION

Based on the definition of retarded Green's function, we obtain the reciprocal space Green's function for multi-layer graphene as:

$$G_{0;l}^{\text{ret}}(\mathbf{m}; \mathbf{k}; E) = \sum_{s=1}^X \frac{D^s(\mathbf{m}; s; \mathbf{k}) D^{l^0}(\mathbf{m}; s; \mathbf{k})}{E + i\epsilon - \epsilon_s^{\text{ns}}(\mathbf{k})}; \quad (9)$$

where  $\epsilon$  is an infinitesimal quantity, and label A or B. By taking the Fourier transform of  $G_{0;l}^{\text{ret}}(\mathbf{m}; \mathbf{k}; E)$  in the first Brillouin zone (1BZ), we can obtain the exact expression of real space multi-layer graphene Green's function,

$$G_0^{\text{ret}}(\mathbf{r}_1; \mathbf{r}_{l^0}^0; E) = \sum_{m=1}^X \int_{1\text{BZ}} d\mathbf{k} G_{0;l}^{\text{ret}}(\mathbf{m}; \mathbf{k}; E) e^{i\mathbf{k} \cdot (\mathbf{r}_1 - \mathbf{r}_{l^0}^0)} \quad (10)$$

Based on the effective-mass approximation, the integral is carried out around six corners in the first Brillouin zone within the low-energy region, which can form two 360° integrals around two inequivalent Dirac points. This method has been well used to study the electronic structure of monolayer and bilayer graphene in our previous works.<sup>13,14</sup> The real space multi-layer Green's function can be obtained as following:

$$\begin{aligned} G_0^{\text{ret}}(\mathbf{r}_{1A}; \mathbf{r}_{l^0A}^0; E) &= \cos[K^{-1}(\mathbf{r}_{1A} - \mathbf{r}_{l^0A}^0)] F_1(\mathbf{r}_{1A} - \mathbf{r}_{l^0A}^0; E); \\ G_0^{\text{ret}}(\mathbf{r}_{1B}; \mathbf{r}_{l^0B}^0; E) &= \begin{cases} \cos[K^{-1}(\mathbf{r}_{1B} - \mathbf{r}_{l^0B}^0)] F_2(\mathbf{r}_{1B} - \mathbf{r}_{l^0B}^0; E) & (l = \text{odd}; l^0 = \text{odd or } l = \text{even}; l^0 = \text{even}) \\ \cos[K^{-1}(\mathbf{r}_{1B} - \mathbf{r}_{l^0B}^0)] F_3(\mathbf{r}_{1B} - \mathbf{r}_{l^0B}^0; E) & (l = \text{odd}; l^0 = \text{even}) \\ \cos[K^{-1}(\mathbf{r}_{1B} - \mathbf{r}_{l^0B}^0)] F_3(\mathbf{r}_{1B} - \mathbf{r}_{l^0B}^0; E) & (l = \text{even}; l^0 = \text{odd}) \end{cases}; \\ G_0^{\text{ret}}(\mathbf{r}_{1A}; \mathbf{r}_{l^0B}^0; E) &= \begin{cases} \sin[K^{-1}(\mathbf{r}_{1A} - \mathbf{r}_{l^0B}^0)] + \mathbf{r}_{1A} \cdot \mathbf{r}_{l^0B}^0 F_4(\mathbf{r}_{1A} - \mathbf{r}_{l^0B}^0; E) & (l^0 = \text{odd}) \\ \sin[K^{-1}(\mathbf{r}_{1A} - \mathbf{r}_{l^0B}^0)] - \mathbf{r}_{1A} \cdot \mathbf{r}_{l^0B}^0 F_4(\mathbf{r}_{1A} - \mathbf{r}_{l^0B}^0; E) & (l^0 = \text{even}) \end{cases}; \\ G_0^{\text{ret}}(\mathbf{r}_{1B}; \mathbf{r}_{l^0A}^0; E) &= \begin{cases} \sin[K^{-1}(\mathbf{r}_{1B} - \mathbf{r}_{l^0A}^0)] - \mathbf{r}_{1B} \cdot \mathbf{r}_{l^0A}^0 F_4(\mathbf{r}_{1B} - \mathbf{r}_{l^0A}^0; E) & (l = \text{odd}) \\ \sin[K^{-1}(\mathbf{r}_{1B} - \mathbf{r}_{l^0A}^0)] + \mathbf{r}_{1B} \cdot \mathbf{r}_{l^0A}^0 F_4(\mathbf{r}_{1B} - \mathbf{r}_{l^0A}^0; E) & (l = \text{even}) \end{cases}; \end{aligned} \quad (11)$$

where

$$\begin{aligned} F_1(\mathbf{r}_{1A} - \mathbf{r}_{l^0A}^0; E) &= \sum_{s=1}^X \sum_{m=1}^X \frac{2S^{-2}}{0} \int_{k_c}^Z dk \frac{k D^2(\mathbf{m}; s; \mathbf{k}) \sin(\frac{m-1}{L+1}) \sin(\frac{m-l^0}{L+1}) J_0(k|\mathbf{r}_{1A} - \mathbf{r}_{l^0A}^0|)}{E + i\epsilon - \epsilon_s^{\text{ns}}(\mathbf{k}) + s[V_2^2 \cos^2(\frac{m}{L+1}) + (rk)^2]^{l=2} g}; \\ F_2(\mathbf{r}_{1B} - \mathbf{r}_{l^0B}^0; E) &= \sum_{s=1}^X \sum_{m=1}^X \frac{2S^{-2}}{0} \int_{k_c}^Z dk \frac{k^3 D^2(\mathbf{m}; s; \mathbf{k}) \sin(\frac{m-1}{L+1}) \sin(\frac{m-l^0}{L+1}) J_0(k|\mathbf{r}_{1B} - \mathbf{r}_{l^0B}^0|)}{E + i\epsilon - \epsilon_s^{\text{ns}}(\mathbf{k}) + s[V_2^2 \cos^2(\frac{m}{L+1}) + (rk)^2]^{l=2} g}; \\ F_3(\mathbf{r}_{1A} - \mathbf{r}_{l^0B}^0; E) &= \sum_{s=1}^X \sum_{m=1}^X \frac{2S^{-2}}{0} \int_{k_c}^Z dk \frac{k^3 D^2(\mathbf{m}; s; \mathbf{k}) \sin(\frac{m-1}{L+1}) \sin(\frac{m-l^0}{L+1}) J_2(k|\mathbf{r}_{1A} - \mathbf{r}_{l^0B}^0|)}{E + i\epsilon - \epsilon_s^{\text{ns}}(\mathbf{k}) + s[V_2^2 \cos^2(\frac{m}{L+1}) + (rk)^2]^{l=2} g}; \\ F_4(\mathbf{r}_{1B} - \mathbf{r}_{l^0A}^0; E) &= \sum_{s=1}^X \sum_{m=1}^X \frac{2S^{-2}}{0} \int_{k_c}^Z dk \frac{k^2 D^2(\mathbf{m}; s; \mathbf{k}) \sin(\frac{m-1}{L+1}) \sin(\frac{m-l^0}{L+1}) J_1(k|\mathbf{r}_{1B} - \mathbf{r}_{l^0A}^0|)}{E + i\epsilon - \epsilon_s^{\text{ns}}(\mathbf{k}) + s[V_2^2 \cos^2(\frac{m}{L+1}) + (rk)^2]^{l=2} g}; \end{aligned} \quad (12)$$

$D(\mathbf{m}; s; \mathbf{k})$  is the normalized factor under the effective mass approximation. It can be obtained from the expression of  $D(\mathbf{m}; s; \mathbf{k})$  by substituting  $V_1^2$  with  $(k)^2$ . Here,  $\epsilon_s = 3\alpha V_1 = 2$ .  $\mathbf{r}_{1A}$  is the angle between  $\mathbf{r}_{1A}$  and x axis.  $K^{-1} = (4/\sqrt{3})/3a; 0$  and  $J_n$  is the type-I n-order Bessel function.  $S = \sqrt{3}/2 \cdot 3a^2 = 2$  is the area of the unit cell in real

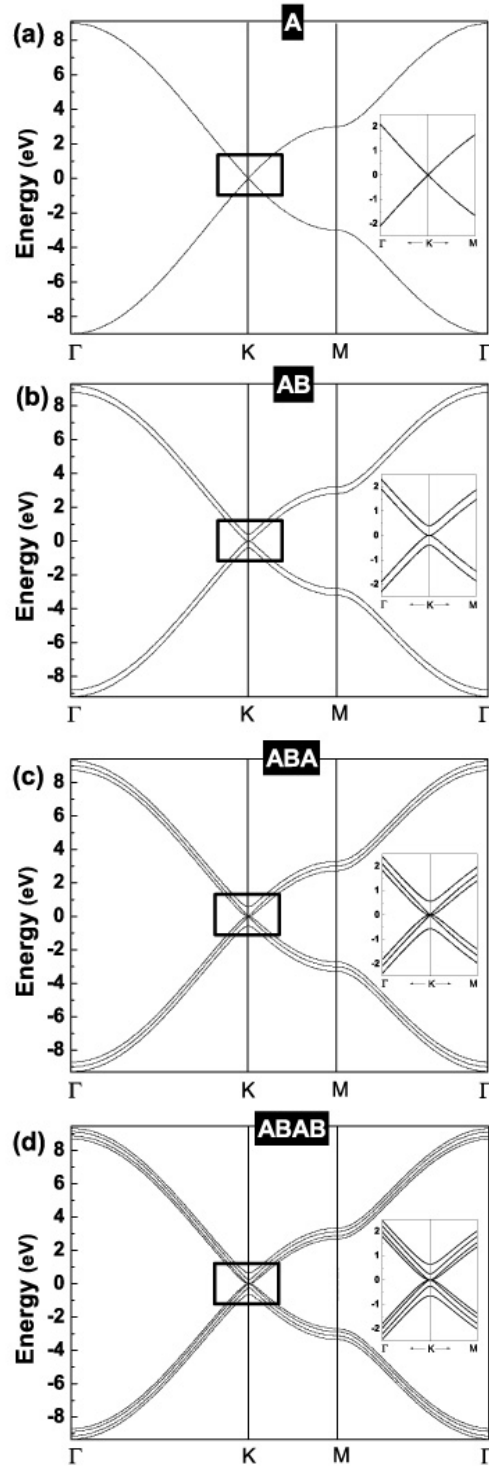


FIG . 2: The band structure of (a) monolayer, (b) bilayer, (c) trilayer and (d) 4-layer bernal stacking graphene along  $\Gamma$ -K-M- $\Gamma$ . The inset is an enlargement of the region indicated by the rectangular around the K point.

space and  $k_c$  is the cutoff wave vector. From Eq.(11) and Eq.(12), it is clear that the real space Green's function of multi-layer graphene is constructed by multiplying two terms: spatially anisotropic and spatially isotropic terms. The spatially anisotropic (three-fold rotational symmetry) can be represented by sine and cosine functions which can be determined from two nonequivalent sets of the Dirac points. The second term including  $F_1, F_2, F_3, F_4$  is spatially isotropic in real space and depends only on the distance between two sites. For  $L=1$  and  $L=2$ , the expression of the Green's function obtained in Eq.(11) and Eq.(12) can directly reduce to our previous results for monolayer and bilayer graphene.<sup>13,14</sup>

#### IV. NUMERICAL RESULTS

##### A. Band structure

As an example of applying the dispersion relation obtained in Eq.(7), we compare the energy band structure of bernal stacking multi-layer graphene involves from monolayer to 4-layer, the corresponding energy bands along the  $KM$  lines in the first Brillouin zone are shown in Fig 2 (a) - 2 (d), respectively. In all the calculations, the Fermi energy is set to  $E_f = 0$ . The following are our observations:

(i) For a monolayer graphene structure as shown in Fig 2 (a), the two bands cross at the  $K$  point leads to the fact that a monolayer graphene is a zero-gap metal. Around the  $K$  point the spectrum is linear as shown in the inset and it is given by  $\epsilon_1^s = s k_p$ . Here,  $k$  is wave vector from the Dirac  $K$  point. Comparing this expression with the relativistic energy expression  $\epsilon = \frac{m^2 c^4 + p^2 c^2}{m}$ , one can see that the dispersion relation of monolayer graphene mimics a system of relativistic Dirac particles with zero rest mass and an effective speed of light  $c = 10^6 m = s$ , which is 300 times smaller than the speed of light in vacuum.

(ii) For a bilayer graphene structure as shown in Fig 2 (b), the number of levels is doubled. The spectrum is clearly no longer linear around the  $K$  point, but is parabolic.  $\epsilon_1^s = V_2 = 2 + s \sqrt{(V_2=2)^2 + (k)^2}$ ,  $\epsilon_2^s = -V_2 = -2 + s \sqrt{(V_2=2)^2 + (k)^2}$ . If moving away from the  $K$  point, the spectrum becomes linear again. In the present calculation by only considering the nearest interaction between layers, we observe that the bands just touch at the  $K$  point. However, a more detailed investigation based on first principle method shows a small overlap and an interaction leading to anticrossings between the conduction and valence bands.<sup>15</sup>

(iii) For a trilayer graphene structure as shown in Fig 2 (c), there are four bands cross at the  $K$  point around zero energy, two of them are linear.  $\epsilon_1^s = \frac{p}{2V_2} = 2 + s \sqrt{(\frac{p}{2V_2}=2)^2 + (k)^2}$ ,  $\epsilon_2^s = s k$ ,  $\epsilon_3^s = -\frac{p}{2V_2} = -2 + s \sqrt{(\frac{p}{2V_2}=2)^2 + (k)^2}$ . It is clear that the band structure around the  $K$  point becomes more complex with increasing number of graphene layers than monolayer and bilayer graphenes. For instance, the number of layers around the Fermi energy at the  $K$  point is doubled in comparison with monolayer and bilayer graphenes. The band diagram can be understood as the combination of band structure in monolayer graphene and in bilayer graphene.

(iv) For a 4-layer graphene, shown in Fig 2 (d), four subbands cross exist at the  $K$  point. From Eq.(7), in the framework of the nearest tight-binding model a general number of the subband cross at the  $K$  point can be deduced. For the number of layers ( $L$ ), there are  $2L$  subband.  $L$  of them cross at the  $K$  point if  $L$  is even, while  $L+1$  subbands cross at the  $K$  point if  $L$  is odd. The additional one subband, existing only when  $\cos(\frac{m}{L+1}) = 0$  (i.e.  $m = \frac{L+1}{2}$ ), is linear.

##### B. Surface Green's Function

In this section, we study the behavior of the top layer Green's function with the changing number of graphene layers ( $L$ ) in detail. From Eq.(11) and Eq.(12), the corresponding real space Green's function of the top layer ( $l = l^0 = 1$ ) are

$$\begin{aligned} G_0^{\text{ret}}(r_{1A}; r_{1A}^0; E) &= \cos K^{-1} (r_A - r_{1A}^0) F_1(j_{1A} - r_{1A}^0; E) \\ G_0^{\text{ret}}(r_{1B}; r_{1B}^0; E) &= \cos K^{-1} (r_B - r_{1B}^0) F_2(j_{1B} - r_{1B}^0; E) \\ G_0^{\text{ret}}(r_{1A}; r_{1B}^0; E) &= \sin K^{-1} (r_A - r_{1B}^0) + r_{1A}; r_{1B}^0 F_4(j_{1A} - r_{1B}^0; E) \\ G_0^{\text{ret}}(r_{1B}; r_{1A}^0; E) &= \sin K^{-1} (r_B - r_{1A}^0) - r_{1B}; r_{1A}^0 F_4(j_{1B} - r_{1A}^0; E) \end{aligned} \quad (13)$$

From previous studies, we find that in the low bias voltage, sites A and B are equivalent for monolayer graphene. They form honeycomb lattice in the STM image. While for a bilayer graphene, sites A and B are inequivalent, and

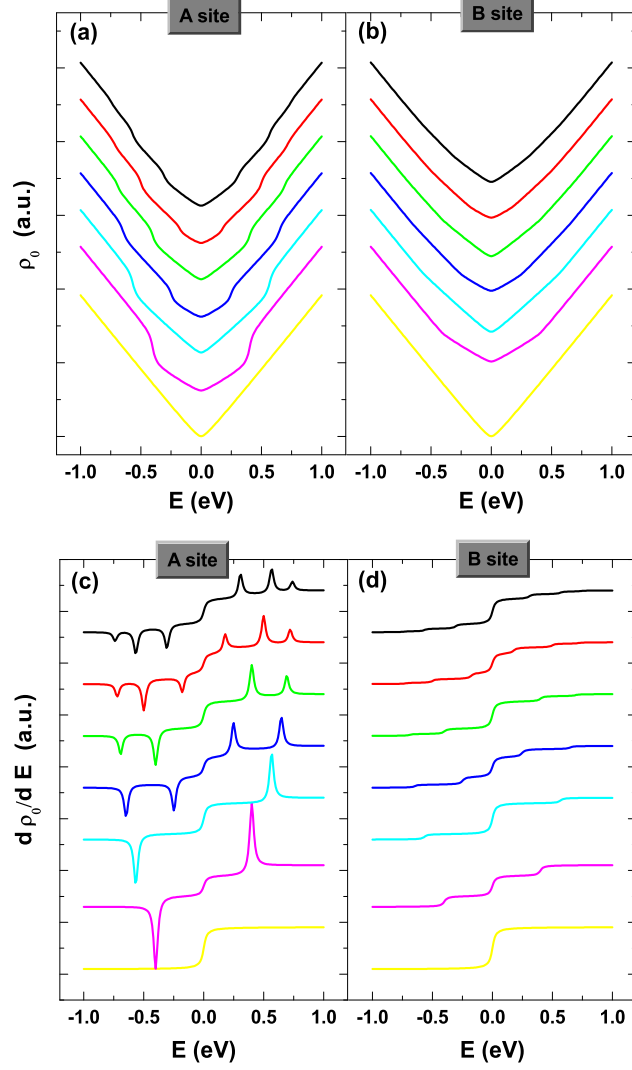


FIG. 3: (color online) (a) and (b) are the LDOS of A and B site at the top layer with different graphene layers (from down to up  $L=1 \sim 7$ ), (c) and (d) are the corresponding derivative of LDOS with energy. To clearly see the difference between them, we shift each curve in (a)–(d) upwards.

the LDOS is residual at site B and they form triangular lattice. Therefore, one direct approach to find the difference among multi-layer graphene is to study the LDOS at sites A and B by changing the number of stacked layers. From Eq.(13), LDOS at sites A and B at the top layer can be expressed as:

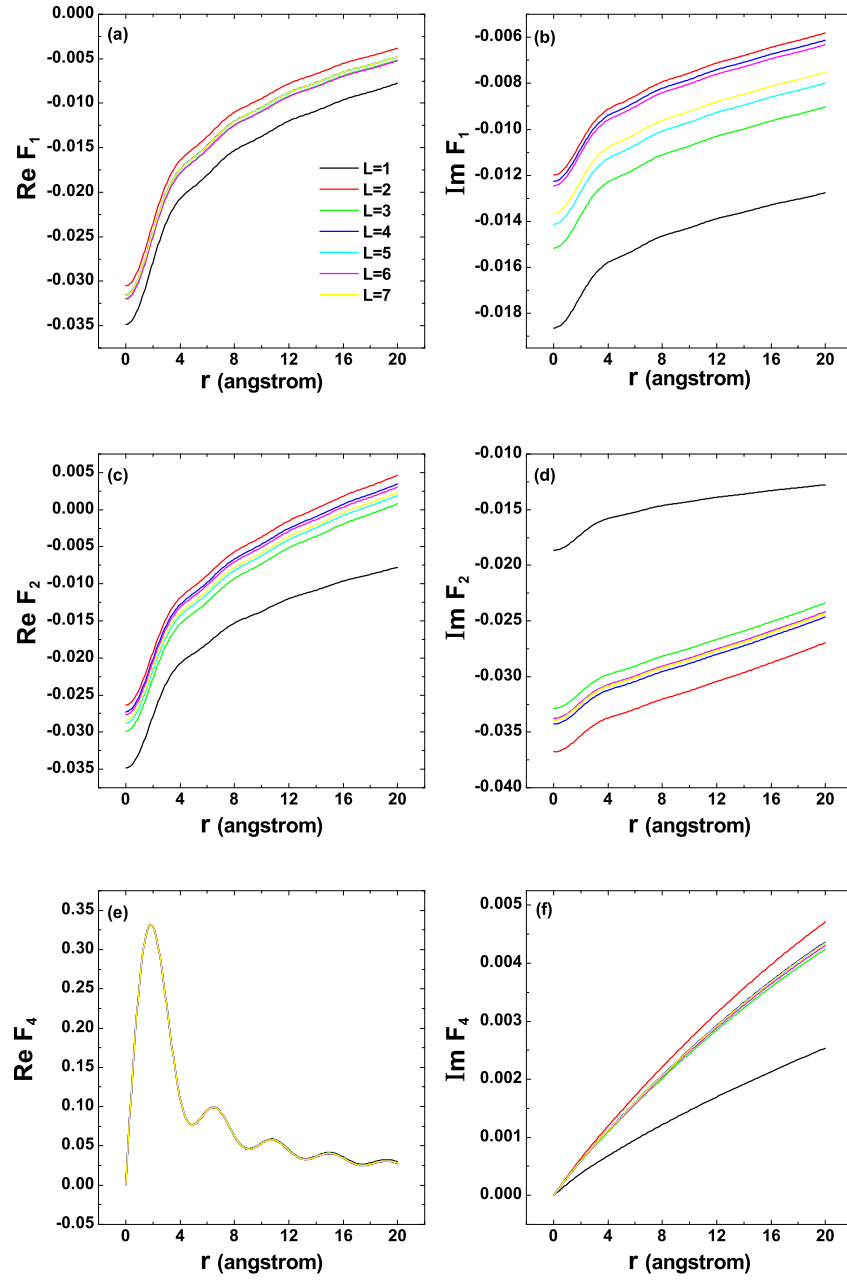


FIG. 4: (color online) Spatially isotropic function  $F_1$ ,  $F_2$  and  $F_4$  of the top layer with different graphene layers ( $L=1$ –7). Here we set  $E = 0.1\text{eV}$ .

$$\begin{aligned}
\rho_0(r_{1A}; E) &= \frac{1}{-i} \text{Im} G_0^{\text{ret}}(r_{1A}; r_{1A}; E) \\
&= \frac{1}{-i} \text{Im} F_1(0; E) \\
\rho_0(r_{1B}; E) &= \frac{1}{-i} \text{Im} G_0^{\text{ret}}(r_{1B}; r_{1B}; E) \\
&= \frac{1}{-i} \text{Im} F_2(0; E)
\end{aligned} \tag{14}$$

Figure 3 (a) and (b) present our numerical results of LDOS at sites A and B with different number of graphene layers. The LDOS for  $L=1$  is linear, which is clearly different from other curves. Starting from  $L=2$ , increasing the number of stacked layer, the LDOS just shows a slight deviation from its bilayer value for both A and B sites. This character means that monolayer graphene is a special case in the family of multi-layer graphene. The relatively weak inter-layer coupling within multi-layer graphene not only inherits some properties from monolayer graphenes, but also solidify some properties between different stacked layers. Detailed studies also find that LDOS at A site converge more slowly than B site with increasing the graphene layers (Twenty layers are needed for the LDOS at A site to converge to its bulk value, while just ten layers needed for B site). LDOS at A site fluctuate more dramatically than that at B site in the process of convergence.

Since the first synthesis of monolayer graphene, except AFM and Raman spectrum<sup>1,10,11</sup>, few method can be used to exactly detect the number of graphene layers. In our work, based on STM second derivative map, we develop a new method to measure graphene layers, which is lacking in the emerging graphene research. From Eq. (14), the derivation of the LDOS with respect to the energy ( $d\rho_0/dE$ ) is proportional to the second derivation of current ( $d^2I/dV^2$ ) in the STM measurement, which corresponds to the excitation of vibrational modes<sup>16</sup>. The results are shown in Fig.3 (c) and (d). The curves are symmetry to the positive and negative energy. So for simplicity, we just consider the positive energy section in the following discussion. For site A, monolayer graphene has no peak, bilayer has one and trilayer has one as well. General relation for the peak number equals  $\text{Int}(L/2)$  (the function  $\text{Int}$  round off the variable to an integer). For  $L$  is even number,  $L$  and  $L+1$  has the same number of peaks, but the peaks for  $L+1$  move towards the high energy direction relative to the  $L$ . With increasing the number of stacked layers, the intensity of the peak become much smaller. For  $L=2$ , the peak height is about  $0.16 \text{ eV}^{-2}$ . While for  $L=14$ , the highest peak reduce to  $0.06 \text{ eV}^{-2}$ . Additionally, the position of small peak is hard to determine when  $L$  become large than 14. Therefore, in the real experiment, only the sample has a few layers (less than 14 layers) may be detected by considering the sensitivity of the STM measurement. For site B, we observe no peak exists, but just step curve. With increasing stack layer, the step become not so clearly anymore.

In the above discussion, we mainly focus on the LDOS of the top layer for the multi-layer graphene. However, to study the propagating behavior of electrons in the top layer of multi-layer graphene, we also need to know the properties of the space isotropic function  $F_1, F_2$ , and  $F_4$  in Eq.(12). The numerical results are shown in Fig.4. For different stacked layer, the curves are almost parallel to each other as shown in Fig.4 (a)–(d). Only the curve for  $L=1$  is clearly differs from the others. In Fig.4 (e), the curves overlap with each other and can not be clearly separated. In Fig.4 (f), all curves start from the same point, but with different slope. The slope of other curves changes slightly except for the curve  $L=1$ . These results indicate that (i) the isotropic function for monolayer graphene is dramatically different from multi-layer graphene; (ii) from  $L=2$  onwards, the isotropic function changes little with increasing the stacked layers. This is consistent with the results obtained from the information of the LDOS study that monolayer graphene is a special case in multi-layer graphene. Starting from bilayer, the electronic structure of graphene changes little when layers increase.

## V. CONCLUSION

In summary, an analytical form of the real space Green's function (propagator) of multi-layer graphene is firstly constructed by using the effective-mass approximation. The Green's function demonstrates elegant spatial anisotropy with three-fold symmetry. Our numerical results show that the monolayer graphene is dramatically different from multi-layer graphene, and it is a special species in the family of graphite. In addition, we provides a new feasible method to identify the graphene layers by measuring the  $d^2I/dV^2$  in STM experiment, or the predicted features based on our simulated results can be used to verified STM measurements. Since multi-layer graphene is described by using the simple non-interactive tight-binding scheme, we are currently investigating how the Coulomb interaction plays a role in electronic structure of multi-layer graphene.

## ACKNOWLEDGMENTS

This work is partially supported by the National Natural Science Foundation of China under Grants No. 10574119, 10674121, 20533030, 20303015, and 50121202 by National Key Basic Research Program under Grant No. 2006CB01200, by the USTC-HP HPC project, and by the SCCAS and Shanghai Supercomputer Center. Work at NTU is supported in part by COE-SUG Grant No. M 58070001. J.C. would like to acknowledge the funding support from the Discovery program of Natural Sciences and Engineering Research Council of Canada (No. 245680).

---

Corresponding author. E-mail: phsqw@ustc.edu.cn

- <sup>1</sup> K. S. Novoselov, A. K. Geim, S. V. Morozov, D. Jiang, M. I. Katsnelson, I. V. Grigorieva, S. V. Dubonos, and A. A. Firsov, *Nature* 438, 197 (2005).
- <sup>2</sup> Yuanbo Zhang, Yan-Wen Tan, Horst L. Stormer and Philip Kim, *Nature* 438, 201 (2005).
- <sup>3</sup> A. C. Ferrari, J. C. Meyer, V. Scardaci, C. Casiraghi, M. Lazzeri, F. Mauri, S. Piscanec, D. Jiang, K. S. Novoselov, S. Roth, and A. K. Geim, *Phys. Rev. Lett.* 97, 187401 (2006).
- <sup>4</sup> Claire Berger, Zhi in Song, Xuebin Li, Xiaosong Wu, Nate Brown, Cecile Naud, Didier Mayou, Tianbo Li, Joanna Hass, Alexei N. M archenkov, Edward H. Conrad, Phillip N. First, Walt A. de Heer, *Science* 312, 1191 (2006).
- <sup>5</sup> M. L. Sadowski, G. Martinez, and M. Potemski, C. Berger and W. A. de Heer, *cond-mat/0605739*.
- <sup>6</sup> J. Scott Bunch, Yuval Yaish, Markus Brink, Kirill Bolotin, and Paul L. McEuen, *Nano Lett* 5, 287 (2005).
- <sup>7</sup> Davy Graf, Francoise Molitor, Klaus Ensslin, Christoph Stampfer, Alain Jungen, Christofer Hierold and Ludger Wirtz, *cond-mat/0607562*.
- <sup>8</sup> K. S. Novoselov, A. K. Geim, S. V. Morozov, D. Jiang, Y. Zhang, S. V. Dubonos, I. V. Grigorieva, and A. A. Firsov, *Science* 306, 666 (2004).
- <sup>9</sup> Claire Berger, Zhi in Song, Tianbo Li, Xuebin Li, Amerom Y. Ogbazghi, Rui Feng, Zhenting Dai, Alexei N. M archenkov, Edward H. Conrad, Phillip N. First, and Walt A. de Heer, *J. Phys. Chem. B* 108, 19 912 (2004).
- <sup>10</sup> A. C. Ferrari, J. C. Meyer, V. Scardaci, C. Casiraghi, M. Lazzeri, F. Mauri, S. Piscanec, D. Jiang, K. S. Novoselov, S. Roth, and A. K. Geim, *Phys. Rev. Lett.* 97, 187401 (2006).
- <sup>11</sup> A. Gupta, G. Chen, P. Joshi, S. Tadigadapa, and P. C. Ekland, *Nano Lett* 6, 2667 (2006).
- <sup>12</sup> S. B. Trickey, F. M. Ller-Plathe, G. H. F. Diierksen, and J. C. Boettger, *Phys. Rev. B* 45, 4460 (1992).
- <sup>13</sup> Z. F. Wang, Ruoxi Xiang, Q. W. Shi, Jinlong Yang, Xiaoping Wang, J. G. Hou, and Jie Chen, *Phys. Rev. B* 74, 125417 (2006).
- <sup>14</sup> Z. F. Wang, Qunxiang Li, Haibin Su, Xiaoping Wang, Q. W. Shi, Jie Chen, Jinlong Yang and J. G. Hou, *Phys. Rev. B* 75, 085424 (2006).
- <sup>15</sup> Sylvain Latil and Luc Henrard *Phys. Rev. Lett.* 97, 036803 (2006).
- <sup>16</sup> C. Didiot, Y. Fagot-Reverat, S. Pons, B. Kierren, C. Chatelain, and D. M alterre, *Phys. Rev. B* 74, 081404(R) (2006).